nature communications

Article

https://doi.org/10.1038/s41467-024-53819-9

Visualizing the topological pentagon states of a giant C_{540} metamaterial

Received: 4 September 2024

Accepted: 21 October 2024

Published online: 07 November 2024

Check for updates

Danwei Liao[1,7], Jingyi Zhang[2,7], Shuochen Wang[1,7], Zhiwang Zhang[1] ✉, Alberto Cortijo[3], María A. H. Vozmediano[3], Francisco Guinea[4], Ying Cheng[1,5] ✉, Xiaojun Liu[1,5,6] ✉ & Johan Christensen[2] ✉

Systems with broken continuous symmetry in ideal lattices cannot be rectified through rearrangement or deformation. Topological metamaterials featuring nontrivial, artificially induced phase transitions have emerged as pivotal constituents for engineering these topological defects, which, until now, have mostly been experimentally realized in linear or planar configurations. Buckminster Fuller lent his name to the C_{60} ball-shaped carbon allotrope, which is not only the roundest molecule in existence but also embodies 3D topological defects. Here, we construct a C_{540} metamaterial composed of interspersed pentagons in a hexagonal network of hollow tubes and cavities. By 3D printing this giant closed-cage topology, the nontrivial state-confinements can be fully controlled and visualized, which, in contrast, in synthesized or naturally found fullerenes, is highly challenging. Thanks to our macroscopic metamaterials approach, we are able to map in real-space topological pentagon states probed by sound waves. Our results show how a seemingly unrelated approach can unveil deep physical understanding in carbon allotropes and potentially in a plethora of other complex systems in the near future.

Buckyballs were first synthesized through laser evaporation but were also found in shungite rocks and carbon-rich stars[1–5]. The topology is recognized for its influence on the electronic characteristics of fullerene molecules, especially in closed-cage systems where they are determined by their inherent topological defects. Topological phases of matter began to see the light of day in connection with Dirac materials, low dimensionality, and strong magnetic fields, yet a landscape of almost ordinary bulk materials has been characterized as topologically nontrivial[6,7]. As opposed to selecting a natural material for its given symmetry and topology, topological metamaterials take a different route toward a targeted purpose, such as robust waveguiding of light or sound[8].

The departure from flatness in graphene is usually caused by unwanted nanoscale structural distortions, e.g., ripples, or intentional strain engineering, which in both cases are accompanied by pseudomagnetic gauge fields, known to significantly alter the electronic properties of graphene and 2D materials in general[9–12]. In particular, these strain-induced gauge fields have been thoroughly brought forward in connection with elastostatic deformations (local curvatures) in rolled-up carbon nanotubes and also in topological defects[13–15]. Extensively studied topological defects lacking rotation symmetry are disclinations formed through Volterra's cut-and-glue process. This prominent approach consists of removing a wedge in a hexagonal flake, after which enormous elastic strain is created, forcing an out-of-plane bend, upon regluing the flake. The fictitious gauge field accounting for such bending, beyond this, also explains electron encircling the associated pentagon defect in analogy with the Aharonov-Bohm effect[16–20].

[1]Department of Physics, MOE Key Laboratory of Modern Acoustics, Collaborative Innovation Center of Advanced Microstructures, Jiangsu Physical Science Research Center, Nanjing University, Nanjing, China. [2]IMDEA Materials Institute, Getafe, Madrid, Spain. [3]Instituto de Ciencia de Materiales de Madrid, CSIC, Cantoblanco, Madrid, Spain. [4]IMDEA Nanociencia, Madrid, Spain. [5]State Key Laboratory of Acoustics, Institute of Acoustics, Chinese Academy of Sciences, Beijing, China. [6]College of Aerospace Engineering, Chongqing University, Chongqing, China. [7]These authors contributed equally: Danwei Liao, Jingyi Zhang, Shuochen Wang. ✉e-mail: zhangzhiwang@nju.edu.cn; chengying@nju.edu.cn; liuxiaojun@nju.edu.cn; johan.christensen@imdea.org

Man-made hopping, chirality by design, or tunable non-Hermiticity are all available attributes, for which topological metamaterials are instrumental[8]. Owing to precise material processing and well-established characterization techniques, 2D photonic and acoustic quantum Hall insulators and quantum spin and valley Hall insulators, have been successfully emulated on the basis of topological metamaterials. These artificial materials, often 3D printed, have also been designed to probe with light[21,22], sound[23–27] or vibrations[28], higher-order corner states[29], topological phase transitions via loss and/or gain[30], and non-Abelian physics[31]. Local obstructions in an order parameter field are topological defects that withstand any continuous lattice deformation. This latest addition to the topological metamaterial family comprises wave-based realizations of topological vortices[32,33], disclinations[34–37], and dislocations[38–40].

Here, we 3D print a giant fullerene sphere containing 540 meta-atoms encompassing a topology with 12 pentagonal among 260 hexagonal faces. Using sound waves, we probe the fullerene sphere with low audio frequencies to highlight both bulk and defect states in the Dirac spectrum. We derive a gauge theory for the 3D-printed fullerene sphere, which is reminiscent of a homogenization approach in traditional metamaterials. This theory treats the structure as a continuum where the lattice disappears, and the defect-pentagons are represented as pure gauge fields. Based on this approach, which shows good agreement with numerical computations, we derive an index theorem after Jackiw-Rossi-Weinberg to discuss the topological origin. Here, we wish to emphasize that this index theorem pertains to the topology of the real-space lattice, which is fundamentally different from the Bloch band topology in periodic systems. Our audible measurements showcase how the topological pentagon-states strongly localize in real space within the C_{540} metamaterial, which, in fact, is 10^8 larger than its carbon counterpart.

Results

Designing a spherical fullerene metamaterial

Borrowed from high-energy physics, we employ a gauge theory to acquire physical insight into the problem. To treat the honeycomb lattice in the effective limit, to first-order linear approximation, we reduce the conventional tight-binding approach to a low-energy Hamiltonian (as shown in Fig. 1a) $\mathcal{H} = v_F \sigma_\mu \partial_\mu$, where v_F represents the Fermi velocity, σ_μ denotes the Pauli matrices, and ∂_μ corresponds to the derivative operator, where $\mu = 1, 2$. In the absence of external fields or particle interactions, the wave function associated with the linear Hamiltonian, i.e., the Dirac spinor Ψ (arrows shown in Fig. 1), advances at the constant phase in the continuum, based on the underlying uniform lattice. To create a truncated icosahedron, we crop ten $\frac{\pi}{3}$ sections from a graphene parallelogram as shown in Fig. 1a. Not only does this establish pentagon disclination defects, moreover, a phase mismatch arises from the broken periodicity and an exchange among two Fermi points, when opposite sides are reattached. Thus, the motion of the Dirac spinor around the pentagon is captured by two vector fields. The first field arises from the intrinsic manifold geometry that is identical to the covariant derivative, which preserves the form invariance of the Dirac equation on the manifold. The second one, inspired by the Aharonov-Bohm effect, accounts for the twelve disclinations whose particle phase exchange can be effectively represented by fictitious gauge fluxes located at the pentagon centers. Reattaching the sheet by excluding the truncated voids is accomplished by collectively combining the twelve non-Abelian vortices representing the pentagons[14]. Thus, the gauge theory approach consists of solving the eigenvalues for a covariant Dirac operator on a spherical surface

$$\mathcal{H}_{\text{sphere}} \Psi = v_F [\sigma^a e_a^\mu (\nabla_\mu - iA_\mu) + \sigma_z \Delta] \Psi = \epsilon \Psi, \tag{1}$$

where the fluxes associated with the twelve pentagons are accounted for by a monopole of charge $g = 3/2$ located at the center of the sphere. This procedure implies that the total flux of all pentagons is spread uniformly at the surface of the sphere[13]. In Eq. (1), σ^a are the Pauli matrices, A_μ is the monopole field, e_μ^a is the zweibein and ∇_μ denotes the covariant derivative on the spherical manifold. From here, we obtain the closed-cage fullerene low-energy spectrum in terms of the

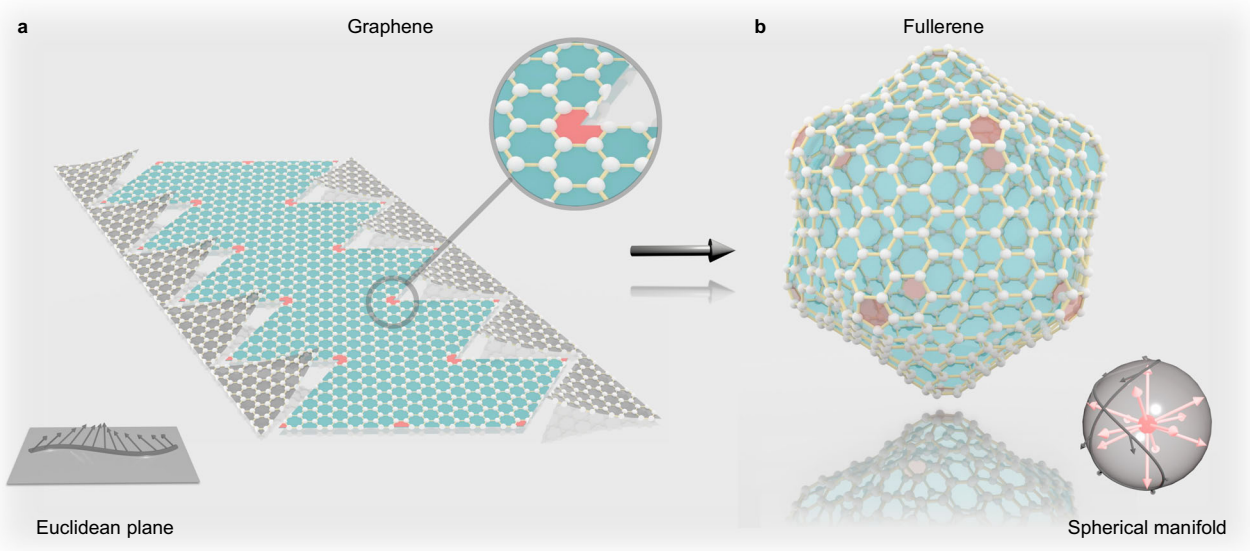

Fig. 1 | Cutting-and-gluing graphene into a fullerene sphere and the associated continuum approximation. a A graphene flake-parallelogram is shown, illustrating a stencil comprising ten $\pi/3$ (gray) cropped sections and parts of twelve (red) pentagons. The light gray plane represents the effective continuum sheet, where the Dirac spinor field is indicated with arrows. **b** Upon removing the cutouts, and gluing opposite sites, the gauge theory introduces fictitious magnetic fluxes accounting for the pentagon disclinations. The closed-cage C_{540} fullerene sphere is folded from the multiple-cut parallelogram, which in the continuum approximation creates a spherical manifold, whose central red monopole has the charge of all individual fluxes accumulated at each pentagon. Its corresponding spinor field creates a phase accumulation across the manifold, arising from the effective monopole and the uniform curvature.

https://doi.org/10.1038/s41467-024-53819-9

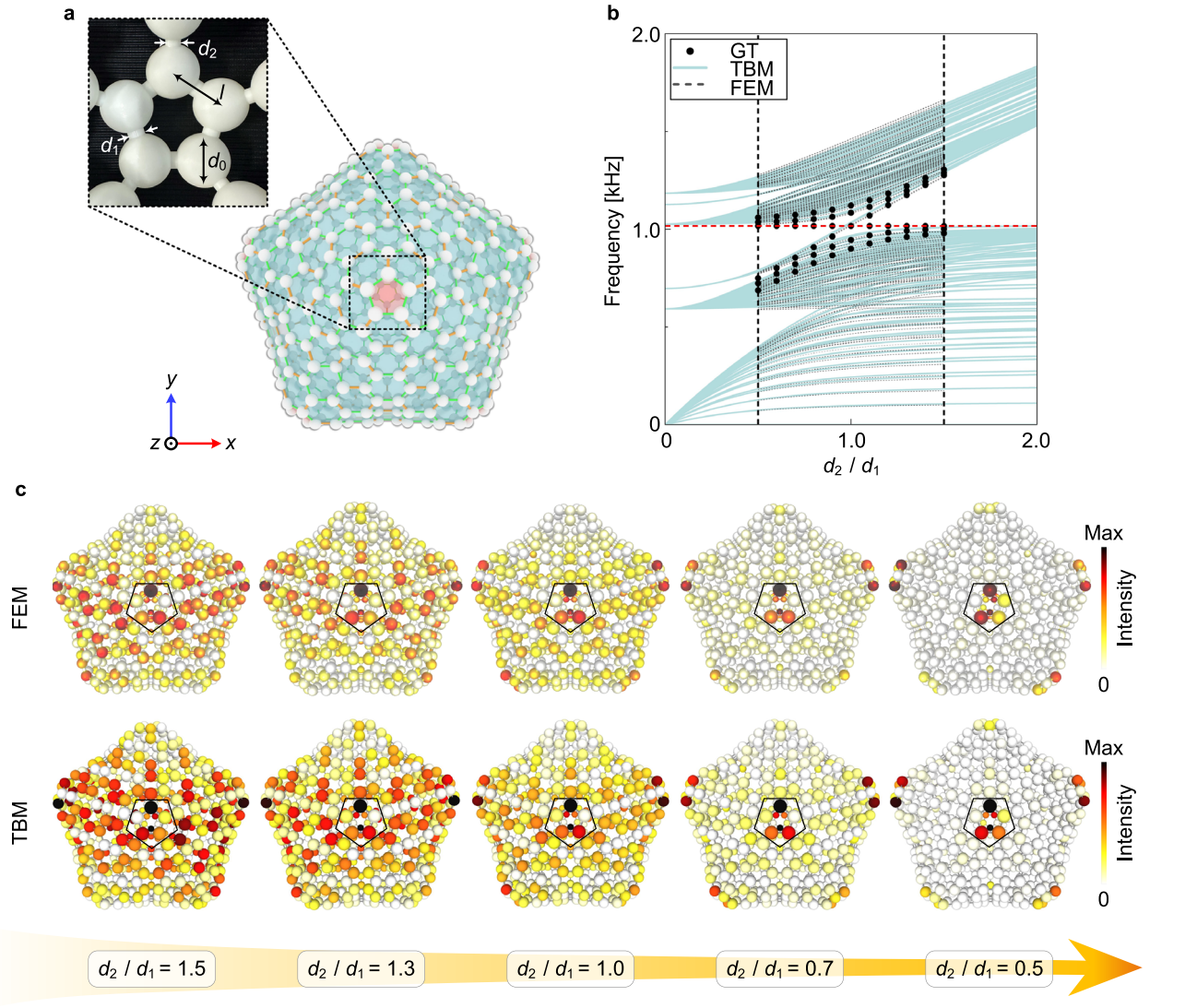

Fig. 2 | Field confinements of topological pentagon states. a Schematic of the C_{540} metamaterial containing hollow spherical cavities interconnected by cylindrical waveguides. **b** The eigenfrequency spectrum is obtained from the gauge theory (GT), a tight-binding method (TBM), and a finite-element method (FEM), showing how the isolated pentagonal and hexagonal resonances evolve with a Kekulé distortion through the tube-hopping diameters d_2/d_1. The horizontal dashed line marks the spectral location of the zero energy. **c** Within the vertically dashed lines in the spectrum of (**b**), we compute, using the FEM and TBM approaches, the acoustic intensity maps for selective values of the tube-hopping ratio.

angular momentum quantum number J through

$$\epsilon = \frac{v_F}{r}\sqrt{\left(J+\frac{1}{2}\right)^2 - g^2 + r^2\Delta^2}, \tag{2}$$

where r represents the average C_{540} radius from tight-binding predictions[18] (see Supplementary Notes 1–3 for details). Beyond this, we also account for a Kekulé distortion Δ in the form of a mass contribution to the Hamiltonian. As we will see later, this term provides additional control over state confinement but poses no additional gauge field contribution. In this spirit, neglecting this part ($\Delta = 0$), after Jackiw-Rossi-Weinberg, we collect the gauge field units,

$$\text{index}\left(\mathcal{H}_{\text{sphere}}\right) = \frac{1}{\pi}\int\int_{S} \nabla \times \mathbf{A} \cdot d\mathbf{S} = 4g, \tag{3}$$

which shows that the zero modes (eigenmodes near the zero-energy level, i.e., the Dirac frequency) exclusively depend on the central monopole charge g, whose strength comes from the individual twelve pentagon fluxes[41,42]. Thus, a couple of zero-energy triples emerge in the low-energy Dirac spectrum, showcasing that these six defect states originate from a topological robust construct. Specifically, the monopole charge of $2g = 3$ yields three zero modes at each Dirac point, totaling six zero modes due to the folding of the valley degeneracy, which forms a double Dirac cone at the center of the first Brillouin zone. We underline that the Jackiw-Rossi-Weinberg index provides the number of zero modes for fullerene-like systems, unlike the invariance characterizing Bloch band topologies.

We begin to test the above-discussed theory by numerically analyzing the C_{540} metamaterial in an acoustic setting. We show that the fundamental knowledge derived in the context of the gauge theory, commonly employed in high-energy and Dirac physics, equally can be transferred to studies concerning sound wave physics (numerical and experimental details are described in "Methods"). Hence, we mimic a fullerene sphere, whose molecules of carbon atoms connect through single and double bonds through a 3D-printed, interconnected hollow network as rendered in Fig. 2a. The carbon atoms are replaced by hollow spheres made of hard

https://doi.org/10.1038/s41467-024-53819-9

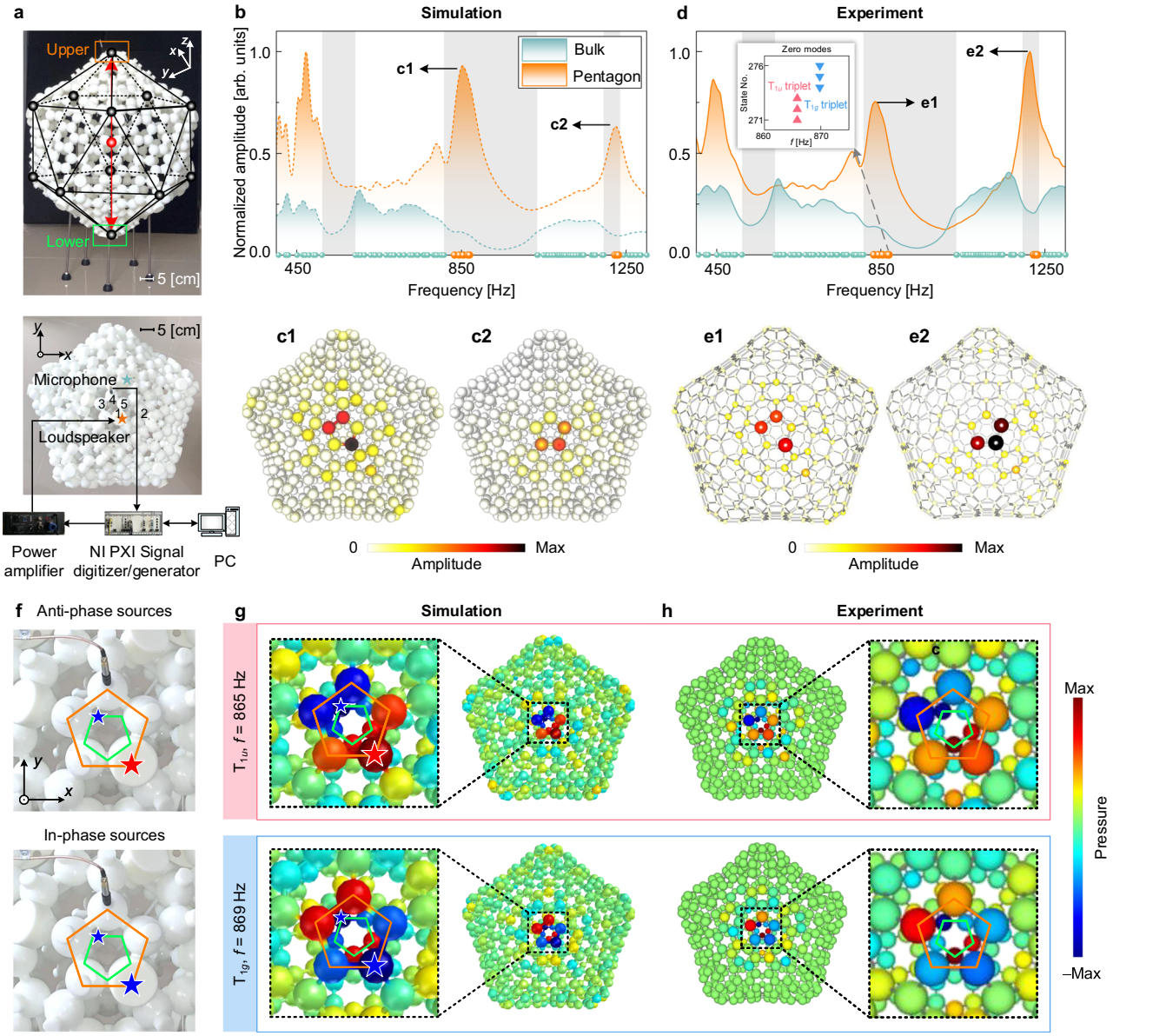

Fig. 3 | Experimentally visualizing the topological defect states of a sonic C_{540} metamaterial. a 3D printed and assembled giant fullerene metamaterial. Black and red dots on the superimposed icosahedron represent the sites of the pentagons and the fullerene center, respectively. The upper and lower pentagons are highlighted to distinguish experimentally the two degenerate triplets of zero modes. A power amplifier is used to launch sound waves through a loudspeaker inserted near the pentagon (orange) and within the bulk of the lattice (cyan). For the spectral measurements in (**d**), the bulk and five averaged pentagon sites were probed with a 1/4 in. condenser microphone whose output was digitized and processed with a PC. For the spatial pressure maps in (**e**), all sites, including and surrounding pentagon defects, were chosen. **b**–**e** Simulated and experimentally observed acoustic pressure amplitude responses, both for bulk and pentagon states within the Dirac spectrum (gaps are highlighted by shades, and the bottom dots denote the eigenfrequencies, with highlighted triplet pair). The acoustic field profiles of the respective defect states are compared from predictions and experimental observations. **f** Overhead perspective onto opposing pentagons that are concurrently excited with opposite (anti-phase) or same phases (in-phase), as indicated by the respective stars. **g** The simulated and (**h**) measured pressure field distributions in response to both anti-phase and in-phase excitations at the frequencies $f = 865$ Hz (T_{1u}) and $f = 869$ Hz (T_{1g}), respectively.

thermoplastic, which are interconnected by cylindrical waveguides of diameters d_1 (green) and d_2 (orange), to account for the non-uniform interatomic bonding. The index theorem predicts six degenerate zero-energy states when $d_1 = d_2$, as depicted in Fig. 2b, which can be grouped into two degenerate triplets based on their inherent symmetry (see Supplementary Note 4). Here, it is seen that the gauge theory agrees very well with the tight-binding approach and numerical simulations, apart from some slight deviations in the continuum approximation. These defect states that reside within the gapped Dirac spectrum, despite being of topological origin, display a rather poor state confinement as finite-element method and tight-binding model predictions showcase in Fig. 2c. To strengthen the confinement and to enable their unequivocal experimental observation, we introduce a mass term to the low-energy Hamiltonian, which slightly shifts the pentagon state from the exact zero energy as seen in Fig. 2b. In this prediction, it is seen how isolated pentagonal and hexagonal ring resonances ($d_2 \to 0$) merge throughout the fullerene lattice within the Dirac dispersion, via the Kekulé distortion as the tube diameter d_2 grows. In other words, the simulations in Fig. 2c display how exceedingly leaky pentagon states can be dragged back to their sites of origin, in the form of highly localized defect states. The tightest acoustic intensity concentration is given when

$d_2 = 0.5d_1$, however, for practical reasons during the fabrication, our parameter of choice for the experimental design will be $d_2 = 0.7d_1$.

Measuring sonic pentagon disclination defects

The fullerene metamaterial assembled from twelve 3D-printed parts is illustrated in Fig. 3a. Under the Mulliken notation[43], T_{1g} and T_{1u} are irreducible representations of triplets belonging to the $\mathcal{I}_h$ icosahedral symmetry group whose structure is superimposed on the fabricated fullerene metamaterial[44–46]. We will later discuss, on the basis of these symmetries, how we experimentally distinguish the characteristics among the triplet pair. Sound waves are launched from a loudspeaker at specific sites, to excite either states in the bulk or confined to the pentagons, from where they are probed by microphones. With an overall diameter of 76.7 cm, we obtain a gapped Dirac spectrum whose locations that are highlighted by shades (see Fig. 3b, d), coincide with band structure simulations in planar acoustic graphene (see Supplementary Note 2). Both in the simulations (Fig. 3b, c) and the measurements (Fig. 3d, e), we inspect two spectra, of which one is probed within 15 arbitrary spherical cavities among the hexagon network, while topological defect excitations originate from averaging the acoustic amplitude among all corners belonging to a single pentagon. The agreeing simulated and measured spectral signatures are captured by their respective acoustic field maps. Interestingly, it is illustrated that the tightly confined pentagon states are both spatially and spectrally distinguishable. We recall that the responsibility of the Kekulé distortion was to reduce the excessive bulk leakage of the topological defects, while slightly off-shifting them away from zero energy. Thus, the fullerene ground states generate a peak at 850 Hz (marked by c1/e1), whereas a higher-order excitation gives rise to a second peak at 1225 Hz (marked by c2/e2), each, having their unique pentagon-confining characteristics as the simulated and measured pressure field maps illustrate. We emphasize losses have been considered in the simulations of Fig. 3, see additional discussion in Supplementary Note 5. The measured zero modes peak, according to the simulation (inset in Fig. 3d), includes two degenerate triplets. With reference to the Hückel molecular orbital theory for a C_{60} buckyball, which shares identical icosahedral symmetry as our giant C_{540} fullerene, one triplet is described by the T_{1g} classification where the orbitals remain unchanged (evenly symmetric) under inversion with respect to the center, conversely for the T_{1u} case, the orbitals change sign (oddly symmetric). In our acoustic context, these symmetry relations translate into pressure wave functions of equal (T_{1g} at 869 Hz) or opposite (T_{1u} at 865 Hz) phases among opposing pentagons. To probe these symmetry properties pertaining to individual triplets, as shown in Fig. 3f, opposing pentagons are excited, each with a loudspeaker, either in or out of phase. The resulting numerical simulations (Fig. 3g) and experimental measurements (Fig. 3h) reveal, upon inversion around the fullerene center, that opposing spatial pressure distributions map symmetrically or asymmetrically in their phases for the acoustic triplets pertaining to the T_{1g} or T_{1u} groups, respectively. In Supplementary Note 6, we discuss the topological robustness against disorder.

Discussion

In summary, we 3D-printed the well-known carbon allotrope, fullerene, in the form of a giant acoustic metamaterial containing 540 meta-atoms. We discussed its topological construct and ensured the tightest possible defect state confinement, realized thanks to a Kekulé lattice distortion. Our sonic approach enabled a hitherto unseen way to experimentally detect and map in real space those pentagonal excitations, which would appear troublesome in its otherwise natural guise. Therefore, we foresee that such an analog platform constitutes an indispensable setting to unlock inaccessible understanding and visualization of nanoscale emergent phenomena. E.g., synthesized buckyballs sheets, i.e., graphullerene, whose electronic band structure comprises localized C_{60} states interacting across their hexagonal planar arrangement, have recently been reported[47,48]. Scaling up this network and other complex carbon allotropes to metamaterial dimensions will only give rise to a deeper understanding of the physics involved when probed by sound or light.

Methods

Numerical simulations

The simulated eigenspectra and eigenfield distributions in Fig. 2 in the main text are obtained through the finite-element-method (FEM) solver COMSOL. The physical models are designed and calculated in the pressure acoustic module, where the air is set with a mass density of $\rho_0 = 1.21\,\mathrm{kg/m^3}$ and a sound speed of $c_0 = 343$ m/s at the temperature of 20 °C. The frequency scanning results shown in Fig. 3b, c are generated by introducing additional loss to the velocity of air as $c = c_0(1 + 0.02i)\,\mathrm{kg/m^3}$, mimicking the intrinsic loss encountered during the experimental measurements. The boundaries of the spheres and the interconnecting cylindrical waveguides are modeled as hard walls. Each meta-atom, i.e., all hollow spheres, has a diameter of $d_0 = 3.6$ cm and a center-to-center distance of $l = 4.5$ cm. Their (inter-cell) diameter d_2 varies owing to the applied Kekulé distortion, while the intra-cell diameter is fixed at $d_1 = 0.75$ cm.

Experimental measurements

The sample was fabricated out of epoxy resin by 3D-printing twelve pieces of the entire fullerene sphere. The experimental measurements were conducted by inserting a speaker into the spherical cavity, with the signals amplified by a power amplifier (BSWA TECH PA300). The pressure fields were detected by inserting condenser microphones (BSWA TECH Model: MPA416) into desired cavities. The output signals were acquired by a digitizer (NI PXI-4499) and processed by the LabVIEW program.

Data availability

All technical details for producing the figures are enclosed in the manuscript and the Supplementary Information. Data are available from the corresponding authors upon request.

Code availability

All technical details for implementing the simulations are enclosed in the manuscript and the Supplementary Information. Codes are available from the corresponding authors upon request.

References

1. Kroto, H. W., Heath, J. R., O'Brien, S. C., Curl, R. F. J. & Smalley, R. E. C_{60}: Buckminsterfullerene. *Nature* **618**, 687–697 (1985).
2. Curl, R. F. & Smalley, R. E. Probing C_{60}. *Science* **242**, 1017–1022 (1988).
3. Kroto, H. Space, stars, C_{60}, and soot. *Science* **242**, 1139–1145 (1988).
4. Buseck, P. R., Tsipursky, S. J. & Hettich, R. Fullerenes from the geological environment. *Science* **257**, 215–217 (1992).
5. Cami, J., Bernard-Salas, J., Peeters, E. & Malek, S. E. Detection of C_{60} and C_{70} in a young planetary nebula. *Science* **329**, 1180–1182 (2010).
6. Hasan, M. Z. & Kane, C. L. Colloquium: Topological insulators. *Rev. Mod. Phys.* **82**, 3045–3067 (2010).
7. Zhang, T. et al. Catalogue of topological electronic materials. *Nature* **566**, 475–479 (2019).
8. Zhang, X., Zangeneh-Nejad, F., Guo, Z., Lu, M.-H. & Christensen, J. A second wave of topological phenomena in photonics and acoustics. *Nature* **618**, 687 (2023).
9. Meyer, J. C. et al. The structure of suspended graphene sheets. *Nature* **446**, 60–63 (2007).
10. Neto, A. C., Guinea, F., Peres, N. M., Novoselov, K. S. & Geim, A. K. The electronic properties of graphene. *Rev. Mod. Phys.* **81**, 109 (2009).

11. Levy, N. et al. Strain-induced pseudo–magnetic fields greater than 300 tesla in graphene nanobubbles. *Science* **329**, 544–547 (2010).
12. Hsu, C.-C., Teague, M., Wang, J.-Q. & Yeh, N.-C. Nanoscale strain engineering of giant pseudo-magnetic fields, valley polarization, and topological channels in graphene. *Sci. Adv.* **6**, eaat9488 (2020).
13. González, J., Guinea, F. & Vozmediano, M. A. H. Continuum approximation to fullerene molecules. *Phys. Rev. Lett.* **69**, 172 (1992).
14. Gonzalez, J., Guinea, F. & Vozmediano, M. A. H. The electronic spectrum of fullerenes from the Dirac equation. *Nucl. Phys. B* **406**, 771–794 (1993).
15. Krishnan, A. et al. Graphitic cones and the nucleation of curved carbon surfaces. *Nature* **388**, 451–454 (1997).
16. Kleman, M. & Friedel, J. Disclinations, dislocations, and continuous defects: A reappraisal. *Rev. Mod. Phys.* **80**, 61 (2008).
17. Lammert, P. E. & Crespi, V. H. Topological phases in graphitic cones. *Phys. Rev. Lett.* **85**, 5190 (2000).
18. Vozmediano, M. A. H., Katsnelson, M. & Guinea, F. Gauge fields in graphene. *Phys. Rep.* **496**, 109–148 (2010).
19. De Juan, F., Cortijo, A., Vozmediano, M. A. H. & Cano, A. Aharonov–Bohm interences from local deformations in graphene. *Nat. Phys.* **7**, 810–815 (2011).
20. Teo, J. C. & Hughes, T. L. Topological defects in symmetry-protected topological phases. *Annu. Rev. Condens. Matter Phys.* **8**, 211–237 (2017).
21. Lu, L., Joannopoulos, J. D. & Soljačić, M. Topological photonics. *Nat. Photonics* **8**, 821–829 (2014).
22. Ozawa, T. et al. Topological photonics. *Rev. Mod. Phys.* **91**, 015006 (2019).
23. Zhang, Z. et al. Structured sonic tube with carbon nanotube-like topological edge states. *Nat. Commun.* **13**, 5096 (2022).
24. He, C. et al. Acoustic topological insulator and robust one-way sound transport. *Nat. Phys.* **12**, 1124–1129 (2016).
25. Lu, J. et al. Observation of topological valley transport of sound in sonic crystals. *Nat. Phys.* **13**, 369–374 (2017).
26. Zhang, X., Xiao, M., Cheng, Y., Lu, M.-H. & Christensen, J. Topological sound. *Commun. Phys.* **1**, 97 (2018).
27. Xue, H., Yang, Y. & Zhang, B. Topological acoustics. *Nat. Rev. Mater.* **7**, 974–990 (2022).
28. Huber, S. D. Topological mechanics. *Nat. Phys.* **12**, 621–623 (2016).
29. Ni, X., Weiner, M., Alu, A. & Khanikaev, A. B. Observation of higher-order topological acoustic states protected by generalized chiral symmetry. *Nat. Mater.* **18**, 113–120 (2019).
30. Hu, B. et al. Non-Hermitian topological whispering gallery. *Nature* **597**, 655–659 (2021).
31. Yang, Y. et al. Non-Abelian physics in light and sound. *Science* **383**, eadf9621 (2024).
32. Chen, C.-W. et al. Mechanical analogue of a Majorana bound state. *Adv. Mater.* **31**, 1904386 (2019).
33. Gao, P. et al. Majorana-like zero modes in Kekulé distorted sonic lattices. *Phys. Rev. Lett.* **123**, 196601 (2019).
34. Rüegg, A. & Lin, C. Bound states of conical singularities in graphene-based topological insulators. *Phys. Rev. Lett.* **110**, 046401 (2013).
35. Wang, Q., Xue, H., Zhang, B. & Chong, Y. Observation of protected photonic edge states induced by real-space topological lattice defects. *Phys. Rev. Lett.* **124**, 243602 (2020).
36. Liu, Y. et al. Bulk-disclination correspondence in topological crystalline insulators. *Nature* **589**, 381–385 (2021).
37. Peterson, C. W., Li, T., Jiang, W., Hughes, T. L. & Bahl, G. Trapped fractional charges at bulk defects in topological insulators. *Nature* **589**, 376–380 (2021).
38. Li, F.-F. et al. Topological light-trapping on a dislocation. *Nat. Commun.* **9**, 2462 (2018).
39. Xue, H. et al. Observation of dislocation-induced topological modes in a three-dimensional acoustic topological insulator. *Phys. Rev. Lett.* **127**, 214301 (2021).
40. Ye, L. et al. Topological dislocation modes in three-dimensional acoustic topological insulators. *Nat. Commun.* **13**, 508 (2022).
41. Jackiw, R. & Rossi, P. Zero modes of the vortex-fermion system. *Nucl. Phys. B* **190**, 681–691 (1981).
42. Weinberg, E. J. Index calculations for the fermion-vortex system. *Phys. Rev. D* **24**, 2669–2673 (1981).
43. Mulliken, R. S. Report on notation for the spectra of polyatomic molecules. *J. Chem. Phys.* **23**, 1997–2011 (1955).
44. Haddon, R. Electronic structure, conductivity and superconductivity of alkali metal doped C_{60}. *Acc. Chem. Res.* **25**, 127–133 (1992).
45. Chung, F. & Sternberg, S. Mathematics and the Buckyball. *Am. Sci.* **81**, 56–71 (1993).
46. Fowler, P. & Ceulemans, A. Electron deficiency of the fullerenes. *J. Phys. Chem.* **99**, 508–510 (1995).
47. Meirzadeh, E. et al. A few-layer covalent network of fullerenes. *Nature* **613**, 71–76 (2023).
48. Pan, F. et al. Long-range ordered porous carbons produced from C_{60}. *Nature* **614**, 95–101 (2023).

Acknowledgements

This work was supported by the National Key R&D Program of China (2022YFA1404501 and 2022YFA1404400), NSFC (12074183, 12104226, 12227809, 12225408 and 12474439), and the Natural Science Foundation of Jiangsu Province (BK20240061 and BK20233001). J.C. acknowledges support from the Spanish Ministry of Science and Innovation through a Consolidación Investigadora grant (CNS2022-135706). M.A.H.V. and A.C. acknowledge financial support from the Spanish Ministerio de Ciencia e Innovación through Grant No. PID2021-127240NB-I00. J.C. and Z.Z. are grateful for stimulating discussions with José Manuel Guevara-Vela.

Author contributions

Z.Z. and J.C. initiated the project and conceived the idea. Z.Z., Y.C., X.L., and J.C. guided the research. D.L. conducted FEM simulations. J.Z., D.L., A.C., M.A.H.V., J.C., and F.G. performed theoretical calculations. D.L., S.W., and Z.Z. designed the experimental setup and conducted the measurements. D.L., J.Z., Z.Z., Y.C., and J.C. wrote the manuscript. All authors contributed to the discussions of the results and the manuscript preparation.

Competing interests

The authors declare no competing interests.

Additional information

Supplementary information The online version contains supplementary material available at https://doi.org/10.1038/s41467-024-53819-9.

Correspondence and requests for materials should be addressed to Zhiwang Zhang, Ying Cheng, Xiaojun Liu or Johan Christensen.

Peer review information *Nature Communications* thanks the anonymous reviewers for their contribution to the peer review of this work. A peer review file is available.